

PlenoptiCam v1.0: A light-field imaging framework

Christopher Hahne and Amar Aggoun

University of Wolverhampton, School of Mathematics and Computer Science

Wulfruna Street, WV1 1LY Wolverhampton, United Kingdom

{c.hahne, a.aggoun}@wlv.ac.uk

Abstract—Light-field cameras play a vital role for rich 3-D information retrieval in narrow range depth sensing applications. The key obstacle in composing light-fields from exposures taken by a plenoptic camera is to computationally calibrate, re-align and rearrange four-dimensional image data. Several attempts have been proposed to enhance the overall image quality by tailoring pipelines dedicated to particular plenoptic cameras and improving the color consistency across viewpoints at the expense of high computational loads. The framework presented herein advances prior outcomes thanks to its cost-effective color equalization from parallax-invariant probability distribution transfers and a novel micro image scale-space analysis for generic camera calibration independent of the lens specifications. Our framework compensates for hot-pixels, resampling artifacts, micro image grid rotations just as vignetting in an innovative way to enable superior quality in sub-aperture image extraction, computational refocusing and Scheimpflug rendering with sub-sampling capabilities. Benchmark comparisons using established image metrics suggest that our proposed pipeline outperforms state-of-the-art tool chains in the majority of cases. The software described in this paper is released under an open-source license offering cross-platform compatibility, few dependencies and a lean graphical user interface to make the reproduction of results and the experimentation with plenoptic camera technology convenient for peer researchers, developers, photographers, data scientists and everyone else working in this field.

Index Terms—plenoptic, light-field, calibration, color transfer

I. INTRODUCTION

THERE is a growing body of literature in the fields of experimental photography [1], [2], medical imaging [3], [4], [5], [6] and machine learning [7] recognizing capabilities offered by light-fields. The probably most influential light-field model in computer graphics was devised by Levoy and Hanrahan [8] who described a light-field to be a collection of ray vectors piercing through two planes stacked behind one another. The intersections of ray vectors at the two planes make up four Cartesian coordinates, which is why light-fields are often referred to as four-dimensional (4-D). In their much celebrated paper, Levoy and Hanrahan demonstrate that the two planes serve as the spatial and angular image domain providing two different light-field representations that can be transferred into each other. Such light-field transformation corresponds to changing the sequential order of the two planes.

Capturing a light-field from a monocular lens is achieved with a single sensor stacked behind an aperture grid [9] such as a Micro Lens Array (MLA). This optical setup is known as a plenoptic camera and can be thought of as accommodating an array of consistently spaced virtual cameras located at the

aperture plane [10]. As opposed to light-fields obtained from an array of multiple cameras, captures from the plenoptic camera need to undergo additional processing to be represented as such [11], [12]. The software described in this paper consolidates preliminary state-of-the-art decoding procedures, while introducing innovations with regards to calibration, resampling, color management and refocusing.

Until today, the landscape of software tools treating plenoptic content has been characterized by heterogeneity. One of the most mature and influential software applications was released by camera manufacturer Lytro in 2012. Lytro’s image processing pipeline remains closed-source and is not publicly maintained since the company shut down business in 2018. In the earlier days of Lytro’s lifetime, independent programmers developed binary file decoders by reverse-engineering Lytro’s file formats [13], [14]. These tools, however, are unable to perform light-field rendering functionalities such as refocusing. Several scientists published methods on how to algorithmically calibrate Lytro’s plenoptic camera within Matlab [11], [12], [15]. These methods are based on the given metadata while concentrating on the micro image center detection, 4-D rearrangement and rectification of radial lens distortions. More recently, research has taken the direction to successfully recover physical information at light-field boundaries [16], [17]. While these studies revealed convincing results, obtaining light-field color consistency as proposed by Matysiak *et al.* [17] requires high computational resources.

Unlike afore-mentioned attempts, PLENOPTICAM is not limited to Lytro file data, but is also capable of handling footage from custom-built plenoptic cameras through its micro image scale estimation. Other innovative features of PLENOPTICAM include a novel and rapid color correction across sub-aperture images, de-vignetting based on least-squares fitting, a first hexagonal artifact removal, and alternatives to resampling and the much popularized refocusing technique, which enables focus manipulation and Scheimpflug rendering of a picture after the fact. These innovations help leverage PLENOPTICAM to accomplish outstanding results, which are validated in this study with standard image metrics. Equipped with generic calibration, decoding and rendering routines, PLENOPTICAM may build the foundation for future research on light-field image algorithms. Novel research goals can be achieved more easily as image scientists can adapt code and focus on their individual idea. The absence of powerful and heavy-weight libraries is intended to keep the dependency list short. Nonetheless, additional libraries can be used as an extension, e.g. to rectify lens distortions and extract depth at a post-processing stage.

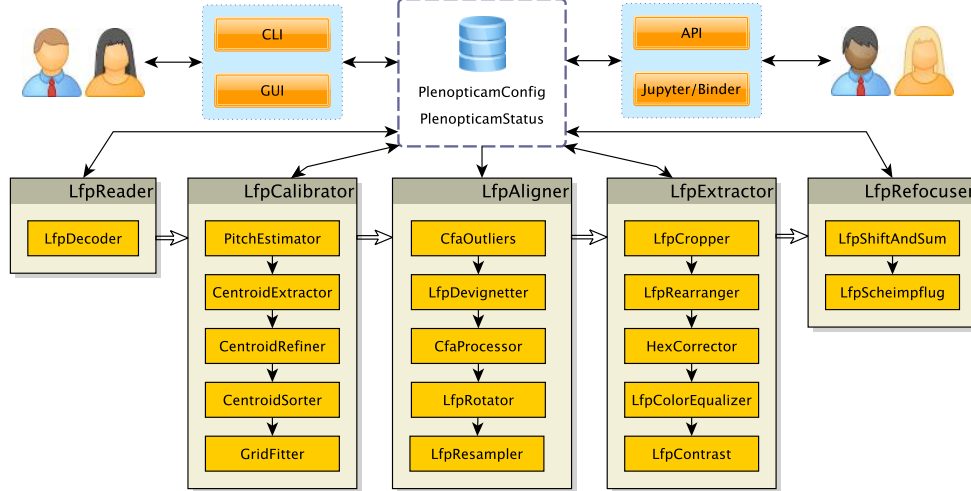


Fig. 1: **Package architecture** with gray blocks representing modules whereas orange blocks indicate essential top-level classes.

Note that PLENOPTICAM can be used in conjunction with the geometry tool PLENOPTISIGN [18] to pinpoint metric object positions in a light-field captured by a plenoptic camera.

The organisation of this paper begins with an introduction to the architectural design of the presented software in Section II, which can be regarded as a roadmap for Section III. Subsections contained in Section III then give insightful details on algorithmic aspects with respect to plenoptic image calibration, sub-aperture extraction and refocusing. A benchmark comparison of results rendered by PLENOPTICAM and other tool chains is carried out in Section IV. Section V draws conclusions, while reflecting on the framework’s potential impact and sketching out ideas for future work.

II. SOFTWARE DESCRIPTION

Usability and reproducibility of the proposed pipeline have been given the same priority as the enhancement of the image quality. Access is provided for a variety of experience levels. PLENOPTICAM offers the possibility to use its Application-Programming-Interface (API), a Graphical-User-Interface (GUI) just as the classical Command-Line-Interface (CLI) for sake of comfort when processing a batch of images. Quick API tests can be made in Jupyter Notebook using Binder [19]. For CLI usage, installation is made possible via the package installer *pip*. At this point, we may refer the interested reader to use the help option via *plenoptiCam -h* for more information on CLI commands. The GUI is made of TKINTER as part of the Python distribution. Configuration settings with several options are documented in the “Help” section in the GUI menu. When feeding Lytro image data, the white image calibration file is selected automatically from tar-archives that correspond to the provided camera file. Instructions on how to generate a tar-archive are found in the documentation. Until now, all code of PLENOPTICAM is written in Python and structured in an object-oriented manner. An architectural scheme of the processing pipeline is sketched in Fig. 1. Objects of a PLENOPTICAMCONFIG and PLENOPTICAMSTATUS class are thought to be singletons

and shared across modules. The processing direction of input image data is from left to right (on module-level) and top to bottom (on class-level) as indicated by the arrows. Note that the diagram in Fig. 1 can be regarded as a roadmap for this section in which the core functionality of each module is presented.

III. MODULE FUNCTIONALITIES

A. *LfpReader*

The LFPREADER module supports standard image file types (*tiff*, *bmp*, *jpg*, *png*) and the more specific raw Lytro file type decoding (*lfp*, *lfr*, *raw*) for Bayer image composition according to the findings by Nirav Patel [13]. For raw data from a Lytro camera, this module exports an image as a *tiff* file in Bayer representation as well as a *json* file containing corresponding metadata which is used for gamma correction. Other image file types are expected to be in sRGB space for gamma handling.

B. *LfpCalibrator*

The fundamental problem we aim to solve when calibrating a plenoptic camera is to register geometric properties of the 4-D micro image representation. This enables a light-field to be rearranged as if captured by an array of multiple cameras with consistent spacing [10]. PLENOPTICAM introduces a novel and generic plenoptic image calibration pipeline with a sequence of steps shown in Fig. 2.

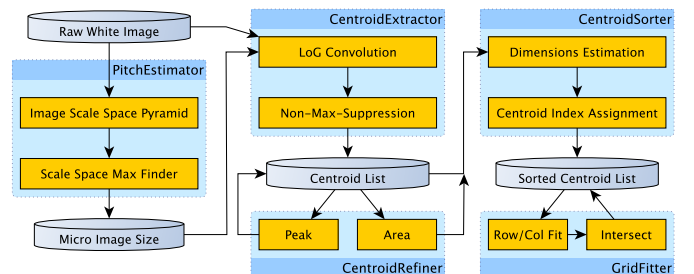


Fig. 2: **Calibration pipeline**

The entire procedure can be sub-divided into pitch estimation, centroid extraction along with optional refinements and centroid sorting of present micro images. To let the pipeline cover multiple types of plenoptic cameras with varying lens and sensor specifications, a blob detector is employed as a first step for analysis of the micro image size.

1) *PitchEstimator*: Based on a white calibration image $I_w(\mathbf{x})$ with arbitrary micro images, we adapt the classical scale space theory [20] for optimized performance using half-octave pyramids [21] denoted by $P(\nu, \mathbf{x})$ and built via

$$\forall \nu, P(\nu + 1, \mathbf{x}) = \mathcal{D}_2(P(\nu, \mathbf{x})) * \nabla^2 G(\sigma, \mathbf{x}) \quad (1)$$

where $\{\nu \in \mathbb{N} \mid \nu < \log_2(\min(K, L))\}$ and K, L are spatial resolutions of $I_w(\mathbf{x})$. Downsampling is represented by $\mathcal{D}_2(\cdot)$ considering the half-octave requirement and $\nabla^2 G(\sigma, \mathbf{x})$ is the Laplacian of Gaussian (LoG) convolution kernel, known as the Mexican hat, which is approximated by the Difference of Gaussians. Each pyramid level at index ν is then a down-scaled LoG-filtered version of the initial white image where $P(0, \mathbf{x}) = I_w(\mathbf{x}) * \nabla^2 G(\sigma, \mathbf{x})$ serves as the first level. The level ν^* exhibits the intensity maximum across all image scales and relates to its σ^* and respective micro image size M given by

$$M \propto \sigma^* = 2^{\nu^*/2} \sqrt{2^{\text{mod}(\nu^*, 2)}}, \text{ where } \nu^* = \underset{\nu}{\arg \max}(P(\nu, \mathbf{x})) \quad (2)$$

and \propto is the equality up to scale for which the proof is found in Appendix A. The base-2 terms account for halved resolutions and the half-octave representation across pyramid levels, respectively. Section IV-A demonstrates that our automatic detection of the micro image size M is an important feature for micro image registration and subsequent light-field alignment processes, which enable PLENOPTICAM to cope with a variety of different MLA and objective lens specifications.

2) *CentroidExtractor*: Initial approximation of Micro Image Centers (MICs) is a key task in plenoptic image registration and has been subject of existing research. An early method developed by Dansereau *et al.* [12] convolves a white image from a Lytro camera with a dedicated kernel of constant size and subsequently analyzes local peaks. Cho *et al.* [11] and similarly Liang *et al.* [22] iteratively apply a morphological erosion operator to white images until a pattern of isolated micro image regions is obtained. Although image erosion facilitates rough centroid detection from intensity maxima, the iterative nature of this approach leaves space for optimizations with regards to speed and robustness. Unlike the previous detection methods, we identify MICs as local extrema in a LoG-convoluted image $I_c(\mathbf{x}) = I_w(\mathbf{x}) * \nabla^2 G(\sigma^*, \mathbf{x})$ by using Non-Maximum-Suppression (NMS) in the form of the 3×3 neighborhood scan. Here the kernel $\nabla^2 G(\sigma^*, \mathbf{x})$ scales with M and helps carve out micro image peaks as it is responsive to the detected feature size. The vector $\mathbf{x} = \{k, l\} \in \mathbb{Z}^2$ consists of image coordinates k, l for the horizontal and vertical direction, respectively. We obtain each MIC denoted as $\mathbf{c} = \{k, l\} \in \mathbb{Z}^2$ by employing Pham's NMS method [23].

3) *CentroidRefiner*: It is important to note that the preliminary CENTROIDEXTRACTOR yields centroids located at integer sensor coordinates. Several studies have shown that

integer coordinate centroids induce artifacts when decomposing a raw plenoptic image to the sub-aperture image representation of a light-field [11], [12], [22]. For accurate light-field decomposition, we refine centroids with sub-pixel precision by taking pixel intensities into account that belong to the same corresponding micro image region \mathcal{R} , which is typically in a range of $M \times M$ size. To obtain sub-pixel precise centroids $\bar{\mathbf{c}} = \{\bar{k}, \bar{l}\} \in \mathbb{R}^2$, we perform coordinate refinement by

$$\bar{k} = \sum_{(k,l) \in \mathcal{R}} I_c(k,l) \cdot k \quad \text{and} \quad \bar{l} = \sum_{(k,l) \in \mathcal{R}} I_c(k,l) \cdot l \quad (3)$$

where $I_c(k, l)$ represents the LoG-convoluted white image. As an alternative to this, we compute area centroids of a binary micro image after applying some threshold such that $I_c(k, l) \in \{0, 1\}$ which then simplifies Eq. (3) to

$$\bar{k} = \frac{1}{|\mathcal{R}|} \sum_{(k,l) \in \mathcal{R}} k \quad \text{and} \quad \bar{l} = \frac{1}{|\mathcal{R}|} \sum_{(k,l) \in \mathcal{R}} l \quad (4)$$

where $|\cdot|$ denotes the cardinality providing the total number of elements within a micro image region \mathcal{R} above a certain threshold value. By default, PLENOPTICAM uses the latter approach given in Eq. (4) as it proves to be the more generic solution for white images suffering from noise or saturation. Figure 14(a) shows an example of detected MICs using this method.

4) *CentroidSorter*: Let $\mathbf{C} = \{\bar{\mathbf{c}}_p \mid p \in \mathbb{N}\}$ be a finite and unordered set of MIC coordinates $\bar{\mathbf{c}}_p = \{\bar{k}, \bar{l}\}$, only little is known about the dimensions and geometric arrangement of the micro lenses. To enable generic calibration for different plenoptic camera models, it is thus necessary to examine fundamental properties of a custom MLA with arbitrary dimensions. Assuming that the ratio of image sensor dimensions K and L will match the aspect ratio of the MLA, we approximate J as the horizontal number of micro lenses via $J = \sqrt{|\mathbf{C}| \times K/L}$ with $|\mathbf{C}|$ as the total number of centroids and similarly the vertical number of micro lenses $H = \sqrt{|\mathbf{C}| \times L/K}$. From these MLA dimensions, it is possible to estimate average distances between micro image centers via K/J and L/H which are used to detect whether the geometric arrangement of micro lenses is hexagonal or rectangular. For a rectangular micro lens packing, these ratios tend to be equal whereas the spacings deviate by a factor of $\sqrt{3}/2$ in the hexagonal case as demonstrated in Fig. 3(b).

Rearranging plenoptic micro images to sub-aperture representation requires MICs to be indexed since their relative positions act as spatial coordinates in the sub-aperture image domain. At this point, however, the order of MICs in the array remains ambiguous. Thus, we seek a procedure that assigns vertical and horizontal micro image indices $j \in \{1, 2, \dots, J\}$ and $h \in \{1, 2, \dots, H\}$ to each centroid $\bar{\mathbf{c}}_{j,h}$. The proposed sort procedure begins with the search for the most upper left centroid $\bar{\mathbf{c}}_{1,1}$ with $j = 1, h = 1$ which is found by the minimum Euclidean distance to the image origin as given by

$$\bar{\mathbf{c}}_{1,1} = \bar{\mathbf{c}}_{p^*}, \text{ where } p^* \in \arg \min_{1 \leq p \leq |\mathbf{C}|} (\|\bar{\mathbf{c}}_p\|_2) \quad (5)$$

and $\|\cdot\|_2$ denotes the ℓ^2 norm. On the basis of an indexed centroid $\bar{\mathbf{c}}_{j,h}$, we search for its spatial neighbor by iterating through \mathbf{C} until finding a candidate $\bar{\mathbf{c}}_p = \{\bar{k}, \bar{l}\}$ that satisfies a window boundary condition $\varphi(\cdot) \in \{0, 1\}$ as seen in

$$\bar{\mathbf{c}}_{j+1,h} = \{\bar{\mathbf{c}}_p \mid \bar{\mathbf{c}}_p \in \mathbf{C} \wedge \varphi(\bar{\mathbf{c}}_{j,h}, \bar{\mathbf{c}}_p) = 1\} \quad (6)$$

which is given by

$$\varphi(\bar{\mathbf{c}}_a, \bar{\mathbf{c}}_b) = \bar{k}_a + \Upsilon < \bar{k}_b < \bar{k}_a + \varepsilon\Upsilon \wedge \bar{l}_a - \Upsilon < \bar{l}_b < \bar{l}_a + \Upsilon \quad (7)$$

where $\Upsilon = M/2$ and ε is a boundary scale parameter set to 3 in the rectangular case and used to cover a hexagonal arrangement otherwise. Boundary parameters thus rely on a previously determined MLA structure and its micro image size M . Note that \bar{k} and \bar{l} may be swapped in Eq. (7) to switch between horizontal and vertical search directions. An exemplary result showing indexed centroids is depicted in Fig. 5.

5) *GridFitter*: At this stage of the calibration pipeline, MICs rely on intensity distributions, which may be affected by a broad range of irregularities arising from the MLA-sensor compound. Based on provided metadata, Dansereau *et al.* [12] compress centroid information by forming a consistently spaced grid, which neglects deviations caused by optical aberrations such as vignetting. Usage of Delaunay triangulation as proposed by Cho *et al.* [11] suits hexagonal arrangements, but becomes impractical when applied to rectangular grids. Instead, we elaborate on a least-squares (LSQ) regression mentioned in a Lytro patent [22]. The spatial coordinates $\bar{k}_{j,h}$ and $\bar{l}_{j,h}$ along rows and columns of MICs are regarded as a function given by

$$\bar{l}_{j,h} = \beta_1 + \beta_2 \bar{k}_{j,h} + \beta_3 \bar{k}_{j,h}^2 \quad (8)$$

which can be represented as matrix \mathbf{X} and vectors $\boldsymbol{\beta}, \mathbf{y}$ by

$$\mathbf{X} = \begin{bmatrix} 1 & \bar{k}_{1,h} & \bar{k}_{1,h}^2 \\ 1 & \bar{k}_{2,h} & \bar{k}_{2,h}^2 \\ \vdots & \vdots & \vdots \\ 1 & \bar{k}_{J,h} & \bar{k}_{J,h}^2 \end{bmatrix}, \quad \boldsymbol{\beta} = \begin{bmatrix} \beta_1 \\ \beta_2 \\ \beta_3 \end{bmatrix}, \quad \mathbf{y} = \begin{bmatrix} \bar{l}_{1,h} \\ \bar{l}_{2,h} \\ \vdots \\ \bar{l}_{J,h} \end{bmatrix} \quad (9)$$

Since \mathbf{X} is not invertible, the equation system is solved via the Moore-Penrose pseudo-inverse denoted as \dagger and given by

$$\mathbf{X}^\dagger = (\mathbf{X}^\top \mathbf{X})^{-1} \mathbf{X}^\top \quad (10)$$

with \top as the matrix transpose so that

$$\boldsymbol{\beta} = \mathbf{X}^\dagger \mathbf{y} \quad (11)$$

yields function fit coefficients in $\boldsymbol{\beta}$ for a row or column of MICs. Centroids are then re-calculated via intersections of two function fits β^j and β^h and re-assigned to spatial coordinates $\bar{\mathbf{c}}_{j,h} = \{\bar{k}, \bar{l}\}$. Enhancements of the herein proposed LSQ grid fit are examined in Section IV-A.

C. *LfpAligner*

1) *CfaOutliers*: In contrast to other pipelines [12], [17], we detect and rectify hot and dead pixels prior to Bayer demosaicing. The reasoning behind our decision is that false intensities are propagated from pixel outliers to adjacent pixels during demosaicing, which may pass unnoticed by a detection method at a later processing stage. To identify pixel candidates, we regard each of the four Bayer channels as a conventional two-dimensional grey scale image $I_B(\mathbf{x})$ and analyze the difference from its Median filtered version as seen in

$$I_R(\mathbf{x}) = I_B(\mathbf{x}) - \mathcal{M}(I_B(\mathbf{x})) \quad (12)$$

where $I_R(\mathbf{x})$ is the reference image that is used for further analysis and $\mathcal{M}(\cdot)$ denotes the Median filter operator. From $I_R(\mathbf{x})$, we obtain the arithmetic mean \bar{I}_R and the standard deviation σ as local statistical measures from a sliding window of $2n + 1$ size to replace potential outliers $I_B(\mathbf{x})$ as follows

$$I_B(\mathbf{x}) = \begin{cases} \mathcal{M}(I_B(\mathbf{x})), & \text{if } I_B(\mathbf{x}) > \bar{I}_R + 4\sigma \\ I_B(\mathbf{x}), & \text{otherwise} \end{cases} \quad (13)$$

where the if clause statement helps detect intensity outliers. Once a condition is fulfilled, nearby intensities in the range of $2n + 1$ are used to replace an outlier. The selection is further constrained by only accepting a small number n of candidates in a $n^2 \times n^2$ window. Without this constrain, many pixels of a saturated image area would be falsely detected as potential outliers.

2) *LfpDevignetter*: In optical imaging, vignetting occurs at non-paraxial image areas as a result of either mechanical blocking of light rays or illumination fall-off from the law of four cosines, which arise from the Lambertian reflectance, pupil size reduction and the distance-dependant inverse square law [24]. Images from a plenoptic camera suffer from vignetting in similar ways whereas the appearance is given in 4-D representation. This image artifact may be treated through a pixel-wise division of the normalized white calibration image [12], [17]. PLENOPTICAM uses this method by default, as it works sufficiently well for white images not severely suffering from noise.

To reduce potential sensor noise, LFPDEVIGNETTER offers an alternative approach to counteract vignetting based on LSQ fitting which is traditionally used in 2-D image processing. The LSQ de-vignetting principle, however, has not yet been applied to raw images of a plenoptic camera. We adapt the classical procedure by iterating through each micro image and performing rectification via division of normalized LSQ fit values to prevent further propagation of noise to the light-field.

The intensity surface of a white micro image $I_m(u, v)$ is approximated by a multivariate polynomial regression. For 2nd order polynomials, this fit function may be given as

$$I_m(u, v) = w_1 + w_2u + w_3v + \dots + w_7u^2v^2 \quad (14)$$

with w as the regression coefficients. Provided the 2-D micro image coordinate indices u and v , this is translated to matrix

form by

$$\mathbf{A} = \begin{bmatrix} 1 & u_1 & v_1 & \cdots & u_1^2 v_1^2 \\ 1 & u_2 & v_2 & \cdots & u_1^2 v_2^2 \\ \vdots & \vdots & \vdots & \ddots & \vdots \\ 1 & u_M & v_M & \cdots & u_M^2 v_M^2 \end{bmatrix}, \mathbf{b} = \begin{bmatrix} I_m(u_1, v_1) \\ I_m(u_1, v_2) \\ \vdots \\ I_m(u_M, v_M) \end{bmatrix} \quad (15)$$

with \mathbf{A} as Vandermonde matrix and vector \mathbf{b} containing micro image intensities. Similar to Eq. (10), we use the Moore-Penrose pseudo-inverse \mathbf{A}^\dagger to obtain fit values $\mathbf{w} = [w_1 \ w_2 \ \dots \ w_7]^\top$ for each micro image by

$$\mathbf{w} = \mathbf{A}^\dagger \mathbf{b} \quad (16)$$

After an estimation of weight coefficients, we divide each micro image of the light field capture by its fitted counterpart from the white calibration image. The herein described method is left optional due to the comparably extensive computational requirements. The effectiveness of the proposed method is demonstrated in Section IV-C.

3) *CfaProcessor*: The CFAPROCESSOR class is dedicated to raw sensor images and can be useful for processing Lytro binary file data for which the featured metadata is considered. Regardless of the file type, the CFAPROCESSOR takes care of debayering, white balancing just as color correction. By default, Menon's algorithm [25] is employed for debayering from the available COLOUR_DEMOSAICING implementation. Findings made by CLIM-VSENSE with regards to highlight processing were adopted by this class as they yield enhanced sub-aperture image quality.

4) *LfpRotator*: At the assembling stage of a plenoptic camera, a micro lens grid is ideally placed so that its tilt angles are in line with that of a sensor array. In the real world, however, this grid may likely be rotated or tilted with respect to the image pixel grid. We suppose that the sensor and MLA planes can be considered parallel by mechanical design, where the back focal plane of a plano-convex MLA coincides with the sensor's image plane once its cover glass touches the planar back vertex of an MLA. To counteract rotations about the z axis, our approach exploits the fact that images exposing aberrations tend to be aberration-free along their central axes. This suggests that a row or column of MICs crossing the image center forms a line that may be a reliable indicator for the MLA rotation angle. Such a central row of MICs $\bar{\mathbf{c}}_{j,\delta} = \{\bar{k}_{j,\delta}, \bar{l}_{j,\delta}\}$ is obtained by $\delta := \lfloor (H-1)/2 \rfloor$ where $\lfloor \cdot \rfloor$ is the nearest integer operation and H the total number of micro lenses in vertical direction. Applying LSQ regression on MICs as proposed in Eqs. (8) to (11) yields $\theta = \arctan(\beta_2)$ as the angle from a slope coefficient β_2 . Rotation of MICs and the respective image is accomplished by multiplying coordinates with a counter-clockwise rotation matrix \mathbf{R}_z about axis z and a translation matrix \mathbf{T} . Transformation matrices are successively multiplied with one another to obtain a rotated centroid set $\bar{\mathbf{c}}'_{j,h} = \mathbf{T}^{-1} \mathbf{R}_z \mathbf{T} \bar{\mathbf{c}}_{j,h}$. An example showing results of the proposed rotation procedure is provided in Fig. 14.

5) *LfpResampler*: Section III-B reveals that micro image centroids $\bar{\mathbf{c}}_{j,h} \in \mathbb{R}^2$ are likely to be found at sub-pixel positions. Taking pixel intensities from nearest integer coordinates

leads to errors and thus image artifacts [11]. It is mandatory to preserve fractional digits of MIC coordinates to accurately decompose a light-field from a plenoptic camera. Therefore, we introduce an interpolation scheme, which retains accuracy by resampling each micro image $I_m(u, v)$ individually.

Figure 3(a) depicts an MIC $\bar{\mathbf{c}}_{j,h}$ and the corresponding bi-cubic coefficients γ based on surrounding pixel centers indexed by (i, j) . Given $\gamma_{i,j}$ as pre-determined weighting coefficients, the sub-pixel precise illuminance surface $A(\cdot)$ at each centroid $\bar{\mathbf{c}}_{j,h} = \{\bar{u}_{j,h}, \bar{v}_{j,h}\} \in \mathbb{R}^2$ is computed via

$$A(u, v) = \sum_{i=1}^4 \sum_{j=1}^4 \gamma_{i,j} \cdot u^{i-1} \cdot v^{j-1} \quad (17)$$

where u, v are indices in the 4×4 image pixel patch and $\bar{\mathbf{c}}_{j,h} = \{\bar{u}_{j,h}, \bar{v}_{j,h}\} \in \mathbb{R}^2$ denote the coordinates of the centroid at which the intensity is interpolated.

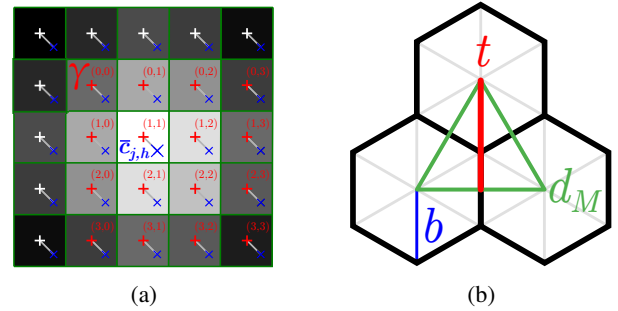


Fig. 3: **Interpolation schemes** with (a) micro image centering and (b) MIC geometry in a hexagonal grid with t as the height and d_M as the side length of an isosceles triangle.

Apart from handling rectangular MLA grids, LFPRESAMPLER supports rectification of hexagonal micro lens arrangements which are detected prior to the centroid-sort procedure. Depending on the hexagonal orientation, the alignment is accomplished by de-interleaving and elongating one dimension at the resampling stage. This shift and stretch is required as a consequence of the hexagonal geometry depicted in Fig. 3(b). We obtain the height of a triangle spanned by three MICs with $t = 3b/2$ and its side length by $d_M = b\sqrt{3}$ which represents the spacing of two MICs as in a rectangular grid. From this, it follows that the sampling density along t is $2/\sqrt{3}$ times higher in relation to d_M . One may note that $d_M/t = \sqrt{3}/3/2$ becomes $2/\sqrt{3}$ after rearranging. Further, it is seen that hexagonal packings imply a displacement of $d_M/2$ for every second MIC coordinate vector. Thus, compensation for hexagonal arrangements may be achieved by translating every other coordinate vector by $d_M/2$ and simultaneously interpolating the number of micro images by factor $2/\sqrt{3}$ along the direction orthogonal to t , which corresponds to the horizontal dimension in case of Lytro cameras.

D. *LfpExtractor*

1) *LfpRearranger*: Based on aligned micro image intensities $E_{f_s} [s_j, u_{c+i}]$ captured at the image sensor plane, the

4-D light-field rearrangement to sub-aperture images $E_i[s_j]$ is achieved by assigning pixels according to

$$E_i[s_j] = E_{f_s}[s_j, u_{c+i}] \quad (18)$$

in the horizontal dimension, which collects micro image pixels at u_{c+i} and relocates them consecutively in a new image array $E_i[s_j]$. Centroid $c = (M-1)/2$ is subject to $\text{mod}(M, 2) = 1$ for each micro image s_j after the alignment. A change in index $i \in \{-c, \dots, c\}$ then controls the relative view position in a light-field and jumps to an adjacent viewpoint whereas index $j \in \{1, 2, \dots, J\}$ iterates through the micro lenses representing the spatial domain. Note that Eq. (18) is equally applied in the vertical direction for complete rendering.

2) *HexCorrector*: While a hexagonal micro lens lattice increases the packing density and thus the spatial resolution, it causes a shortcoming at the rectangular resampling stage, becoming visible as fringe patterns along straight object edges in sub-aperture images (see Fig. 10 for details). This is a result of hexagonal resampling, shifting every other row by half the spacing while actual object edge transitions may move to incorrect positions causing a visual zipper-like appearance. To the best of our knowledge, we are the first to recognize and tackle that issue. To achieve this, it is essential to identify pixel candidates affected by this hexagonal shift artifact.

For an analytical detection, we compose two auxiliary images $E[\hat{s}_j]$ and $E[\check{s}_j]$ by de-interlacing, i.e. taking every other row, of a sub-aperture image $E_i[s_j]$ where $E[\hat{s}_j]$ represents unshifted (ground-truth) pixel vectors and $E_i[\check{s}_j]$ the shifted ones. Then we deduct unshifted pixels from their shifted neighbors via

$$\tilde{V}_i[\check{s}_j] = E_i[\check{s}_j] - E_i[\hat{s}_j] \quad (19)$$

to extract local variances in an image vector $\tilde{V}_i[\check{s}_j]$ containing strong responses at edges parallel to the shift and stretch direction. To remove edges of real objects, we further subtract the magnitude of the partial derivative $\partial_s E_i[\hat{s}_j]$ by

$$\bar{V}_i[\check{s}_j] = |\tilde{V}_i[\check{s}_j]| - |\partial_s E_i[\hat{s}_j]| \quad (20)$$

to leave real edges out of consideration. At this stage, we assume $\bar{V}_i[\check{s}_j]$ to exhibit peaks for potential candidates which we isolate from noisy responses via thresholding with τ by

$$V_i[\check{s}_j] = \begin{cases} 1, & \text{if } \bar{V}_i[\check{s}_j] > \tau \\ 0, & \text{otherwise} \end{cases} \quad (21)$$

To further exclude false positives along the shift and stretch direction, we reject candidates not being part of a consecutive sequence of minimum length 4 in an unraveled vector $V_i[\check{s}_j]$. This way it is ensured that treated areas have sufficient length to be visually recognized. Finally, the remaining candidates in $V_i[\check{s}_j]$ are used to make substitutions in $E_i[s_j]$ by

$$E_i[s_j] = \begin{cases} \frac{1}{|\mathcal{R}|} \sum_{h \in \mathcal{R}} E_i[t_h], & \text{if } V_i[\check{s}_j] = 1 \\ E_i[s_j], & \text{otherwise} \end{cases} \quad (22)$$

for each $j \in \{1, 2, \dots, J\}$ and where t_h denotes the vertical dimension (orthogonal to s_j) in a surrounding region \mathcal{R} of a 2-D sub-aperture image. The effectiveness of this solution is demonstrated in Fig. 10.

3) *LfpColorEqualizer*: Lens components generally expose a gradual intensity decline toward image edges caused by four cosine terms [24]. With a micro image fully covered by the sensor, this illumination fall-off is spread across a relatively small group of Bayer pattern pixels that are merged during demosaicing. Visible intensity variances in off-axis sub-aperture views are thus a result of vignetting at the micro image level that we aim to rectify with the LFP COLOREQUALIZER module. Recent research dealt with enhancing the consistency of light intensities across light-field views [17]. The idea behind this concept is to propagate trusted intensities from paraxial image areas that expose no severe image aberrations to sub-aperture images located at the edge of a light-field. It can thus be used in addition to de-vignetting by utilizing the information redundancy within the light-field. In a recent study, Gaussian Mixture Models (GMMs) were employed in conjunction with disparity correspondences computed at a preceding stage to reduce color inconsistencies [17]. However, the authors note that their procedure requires a high computational load (240 mins per light-field) due to the many computational steps involved.

To overcome this limitation, we introduce linear mappings based on probability distributions. A well known classical method in image processing to achieve this is formally known as Histogram Matching (HM). HM proves to be advantageous when applied to light-fields as it is invariant of the texture so that it preserves parallax information while requiring relatively little computational effort as opposed to iterative methods like k-means. Besides this method, we employ a recent advance in image color transfer that is based on the Monge-Kantorovich-Linearization (MKL). MKL has been introduced to the field of image processing by Pitié and Kokaram [26] to facilitate automatic color grading in media production. As of now, the Monge-Kantorovich principle has not been applied to light-field image processing, especially in the context of color equalization among light-field views acquired from a plenoptic camera. Due to its linearization of Multi-Variate Gaussian Distribution (MVG D) modeling, we expect MKL to outperform HM in terms of accuracy while reducing the computational complexity imposed by the GMM method [17]. Mathematical details of our implemented HM-MKL compound are presented hereafter.

Similar to other literature [27], we denote $f(r_k)$ to be a Probability Density Function (PDF) with r_k as color channel intensities of a sub-aperture image $E_i[s_j]$ given by

$$f(r_k) = \frac{\eta(r_k)}{JH}, \quad \forall k \in \{1, 2, \dots, \mathcal{L}\}. \quad (23)$$

Here $\eta(\cdot)$ yields the number of pixels with intensity level k where \mathcal{L} is the level maximum. The histogram is normalized by JH as the total pixel count of the sub-aperture image. From this we compute $F(r_k)$ as the Cumulative Density Function (CDF) which is obtained using an auxiliary index ϵ via

$$F(r_k) = \sum_{\epsilon=1}^k f(r_\epsilon), \quad \forall k \in \{1, 2, \dots, \mathcal{L}\}. \quad (24)$$

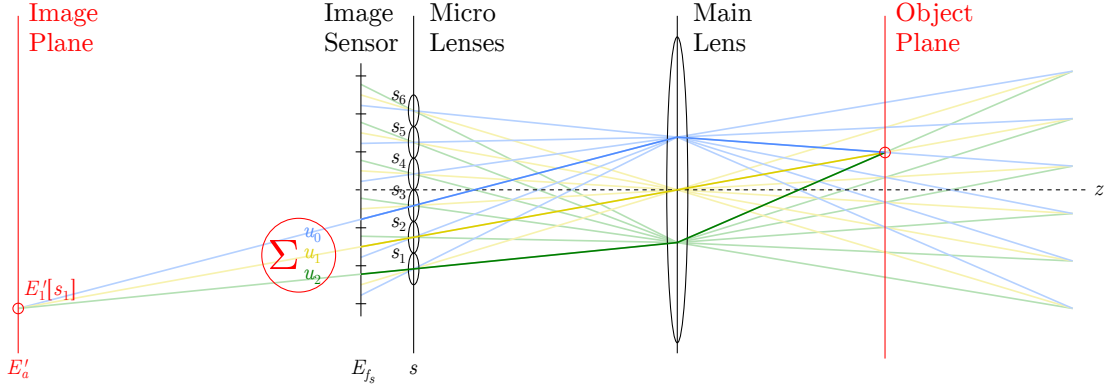


Fig. 4: **Refocusing concept** with chief ray intersections indicating object and image plane for a recovered point $E'_1[s_1]$.

To match $F(r_k)$ as a source CDF with that of a target $T(z_q)$, we perform a pixel mapping via the inverse T^{-1} that satisfies $F(r_k) = T(z_q)$ and reads

$$z_q = T^{-1}(F(r_k)) \quad (25)$$

where each value r_k gets assigned a new value z_q from the corresponding probability map T^{-1} which is implemented as a discrete lookup table. While this channel-wise mapping is straightforward, it fails to sufficiently transfer color intensities at the level satisfying our human visual perception.

It is therefore our motivation to determine an optimal PDF transport plan using linear algebra. Due to the statistical nature of (r, g, b) intensity distributions, we regard the source $\mathbf{r} = [r_k^{(r)}, r_k^{(g)}, r_k^{(b)}]^\top$ and target $\mathbf{z} = [z_q^{(r)}, z_q^{(g)}, z_q^{(b)}]^\top$ as correlated color channel MVGDs given by

$$\mathcal{N}(\mathbf{r}; \boldsymbol{\mu}_r, \boldsymbol{\Sigma}_r) = \frac{\exp(-\frac{1}{2}(\mathbf{r} - \boldsymbol{\mu}_r)^\top \boldsymbol{\Sigma}_r^{-1}(\mathbf{r} - \boldsymbol{\mu}_r))}{\sqrt{(2\pi)^{\text{rank}(\boldsymbol{\Sigma}_r)} |\boldsymbol{\Sigma}_r|}} \quad (26)$$

where $\boldsymbol{\Sigma}_r$ and $\boldsymbol{\Sigma}_z$ denote covariance matrices while $\boldsymbol{\mu}_r$ and $\boldsymbol{\mu}_z$ are the mean vectors of \mathbf{r} and \mathbf{z} , respectively. A desired transfer requires the PDFs to be equal and thus fulfill the condition $\mathcal{N}(\mathbf{z}; \boldsymbol{\mu}_z, \boldsymbol{\Sigma}_z) \propto \mathcal{N}(\mathbf{r}; \boldsymbol{\mu}_r, \boldsymbol{\Sigma}_r)$, which yields

$$(\mathbf{z} - \boldsymbol{\mu}_z)^\top \boldsymbol{\Sigma}_z^{-1}(\mathbf{z} - \boldsymbol{\mu}_z) = (\mathbf{r} - \boldsymbol{\mu}_r)^\top \boldsymbol{\Sigma}_r^{-1}(\mathbf{r} - \boldsymbol{\mu}_r) \quad (27)$$

after dropping the constant leading terms. Using the pseudo-inverse \dagger from Eq. (10), we arrange the above equation to

$$(\mathbf{z} - \boldsymbol{\mu}_z) = ((\mathbf{z} - \boldsymbol{\mu}_z)^\top \boldsymbol{\Sigma}_z^{-1})^\dagger (\mathbf{r} - \boldsymbol{\mu}_r)^\top \boldsymbol{\Sigma}_r^{-1}(\mathbf{r} - \boldsymbol{\mu}_r) \quad (28)$$

As we seek a compact transfer matrix, we define \mathbf{M} to be

$$\mathbf{M} = ((\mathbf{z} - \boldsymbol{\mu}_z)^\top \boldsymbol{\Sigma}_z^{-1})^\dagger (\mathbf{r} - \boldsymbol{\mu}_r)^\top \boldsymbol{\Sigma}_r^{-1} \quad (29)$$

so that after substitution and rearranging, Eq. (28) becomes

$$\mathbf{z} = \mathbf{M}(\mathbf{r} - \boldsymbol{\mu}_r) + \boldsymbol{\mu}_z \quad (30)$$

for the forward transfer. The determination of \mathbf{M} is key for an optimal transport. We utilize Pitié's findings who employed MKL with $\mathbf{M}^\top \boldsymbol{\Sigma}_z^{-1} \mathbf{M} = \boldsymbol{\Sigma}_r^{-1}$ and which is given by

$$\mathbf{M} = \boldsymbol{\Sigma}_r^{-1/2} (\boldsymbol{\Sigma}_r^{1/2} \boldsymbol{\Sigma}_z \boldsymbol{\Sigma}_r^{1/2})^{1/2} \boldsymbol{\Sigma}_r^{-1/2} \quad (31)$$

It is worth noting that Pitié elaborated on a variety of other solutions for \mathbf{M} , e.g. Cholesky decomposition, among which

MKL proved to be the most successful in terms of accuracy [28]. An experimental evaluation of the proposed HM, MKL and HM-MKL methods is carried out in Section IV.

E. LfpRefocuser

The LFPREFOCUSER module covers algorithms concerned with the computational change of image focus based on light-field images. To achieve this, LFPREFOCUSER offers 3 different mechanisms on how to conduct refocusing. The fundamental technique is the conventional shift and sum method as originally presented by Isaksen *et al.* [29] who employed a light-field taken by an array of cameras. Transferring this concept to sub-aperture images $E_i[s_j]$, a refocused image $E'_a[s_j]$ with synthetic focus parameter a is given by

$$E'_a[s_j] = \sum_{i=-c}^c E_i[s_{j-a(c+i)}], \quad a \in \mathbb{Q} \quad (32)$$

for the 1-D case leaving out variables for the vertical domain. A refinement option in PLENOPTICAM enables sub-pixel precision in refocusing via upsampling each sub-aperture image before integration. This not only increases the spatial resolution, but also allows for sub-sampling the refocused depth range along the optical axis of the main lens.

As an alternative to Eq. (32), shift and sum can be accomplished from an aligned micro image representation $E_{f_s}[s_j, u_{c+i}]$ as a starting point, which then writes

$$E'_a[s_j] = \sum_{i=-c}^c E_{f_s}[s_{j+a(c-i)}, u_{c+i}], \quad a \in \mathbb{Q} \quad (33)$$

and can be thought of as employing an interleaved convolution kernel as shown in our previous work examining FPGA-based refocusing practicability [30]. The concept behind Eq. (33) is illustrated in Fig. 4 with the aid of chief rays and paraxial optics for a more intuitive understanding of computational refocusing. Interested readers may note that refocused distances can be pinpointed in space, using this model [2], [18].

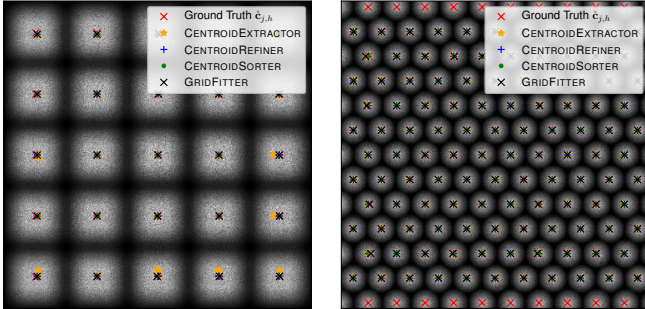
The refocuser module features the LFPSCHEIMPFLUG class which mimics the identically named principle on a computational level. Tilting the refocused plane is achieved through a fusion of spatial image areas from monotonically varying synthetic focus parameter a . This enables the LFPSCHEIMPFLUG

module to render tilted focus along horizontal, vertical and both diagonal image corner-to-corner directions, where focal start and end points rely on provided a . Figure 18 depicts a plenoptic-based photograph exhibiting the Scheimpflug effect.

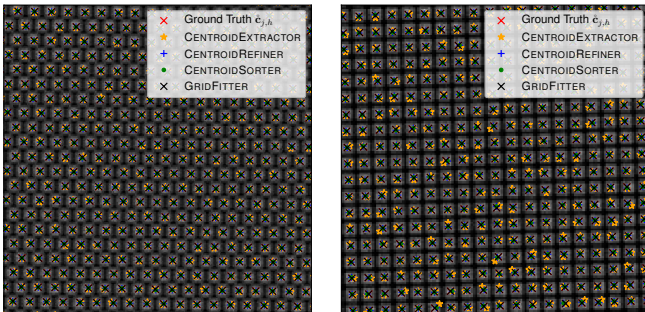
IV. RESULTS

A. Calibration

PLENOPTICAM’s generic calibration capability is tested under different scenarios with micro images varying in size, number, rotation angle, packing geometry and pixel noise. Our proposed calibration pipeline is validated through synthesized data featuring respective ground-truth references. Results are depicted in Fig. 5 for visual inspection.



(a) $M = 143, J = H = 5, \theta = 0^\circ$ (b) $M = 65, J = H = 13, \theta = 0^\circ$



(c) $M = 11, J = H = 64, \theta = 1^\circ$ (d) $M = 8, J = H = 90, \theta = -2^\circ$

Fig. 5: **Auto-calibration results** from synthetic data showing noisy micro images varying in size with square pupil and rectangular packing in (a); circular pupil and hexagonal packing in (b); dense, tilted hexagonal packing in (c); and dense, tilted rectangular packing in (d).

To analyze the PITCHESTIMATOR as an early stage of the pipeline, scale space maxima along ν are presented from the examples shown in Fig. 5(a) to (d).

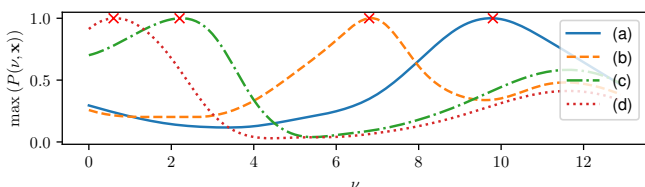


Fig. 6: **Scale maxima analysis** from PITCHESTIMATOR with pyramid data from Fig. 5 where crosses signify respective ν^*

For a quantitative examination of the centroid accuracy, we use C as a deviation metric in pixel unit given by

$$C = \frac{1}{JH} \sum_{j=1}^J \sum_{h=1}^H \|\hat{c}_{j,h} - \bar{c}_{j,h}\|_2 \quad (34)$$

for each of our centroid detection methods. Here $\hat{c}_{j,h}$ represents actual coordinates from the image synthesis that act as a ground-truth. Numerical results from Eq. (34) in Fig. 5 are provided in Table I. Figure 5(a) suggests that approximates from CENTROIDEXTRACTOR appear significantly off with regards to the ground-truth while subsequent refinement stages enhance the accuracy. Closer inspection reveals that the CENTROIDEXTRACTOR may yield several centroids for a micro image suffering from noise. This is a side effect of NMS which would have been of greater concern if white images were not convolved with $\nabla^2 G(\sigma^*, \mathbf{x})$ prior to NMS, as this proves to cancel out false maxima. Candidates passing through LFPEXTRACTOR thus tend to be close to the ground-truth.

TABLE I: Centroid deviation C in [px]

Fig. 5	Stage 1	Stage 2		Stage 3	Stage 4
	CENTROID EXTRACTOR	CENTROIDREFINER <i>peak</i>	<i>area</i>	CENTROID SORTER	GRID FITTER
(a)	6.171	2.984	1.941	1.849	2.031
(b)	0.961	0.227	0.220	0.207	0.579
(c)	0.873	0.393	0.219	0.219	0.053
(d)	0.896	n.a.	0.291	0.288	0.042

From the results in Table I, it follows that the CENTROIDREFINER uses Eq. (4) by default as opposed to Eq. (3) which propagates more imprecise coordinates to subsequent procedures. The reason behind CENTROIDSORTER yielding better results in Table I is that it merges centroids belonging to the same micro image. Usage of GRIDFITTER is left optional as it proves to reduce deviations only in certain cases, e.g. tilted MLAs or for a large number of micro images. These improvements arise from larger data sets resulting in lower residuals as well as slight MLA rotations that help stabilize the fits. One may note that vignetting causes off-center micro images to be of non-radially symmetric shape, shifting detected centers away from their actual physical counterparts. To work against this displacement, interested readers are referred to the methods proposed by peers [31], [22], [32], [33].

B. Sub-aperture images

The central view of a light-field generally suffers the least of aberrations and thus, exposes best image quality. Figure 8 depicts decoded central views of light-field photographs from the available IRISA dataset [34] rendered by state-of-the-art plenoptic imaging pipelines for comparison. Closer inspection reveals that central views from LFTOOLBOX v0.5 appear brighter, but - in contrast to the others - fail to preserve bright image details. For a quantitative assessment of the different pipelines, we seek a metric serving as an objective measure. Since central sub-aperture images lack ground-truth references, we employ a widely accepted no-reference-based technique named *Blind Reference-less Image Spatial Quality Evaluator* (BRISQUE) [35] from the *pybrisque* implementation [36]. Scores from the BRISQUE metric are presented in

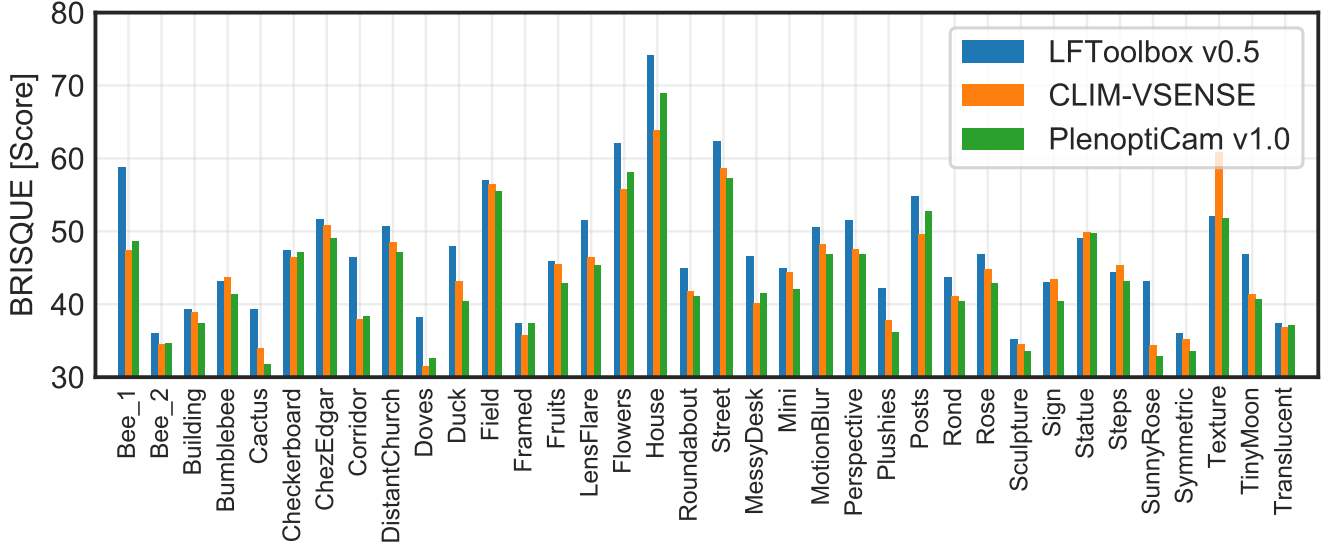


Fig. 7: **Analysis of central sub-aperture images** from [34] along the horizontal axis and BRISQUE metric scores along the vertical axis where lower values signify higher quality. Our tool chain outperforms others in 24 out of 36 images in total.

Fig. 7. Light-field denoising as borrowed by [17] was left out in the evaluation as it is considered equally effective for each pipeline and thus, not crucial for the decomposition. For our benchmark comparison, all pipelines are set to render with de-vignetting, color and sRGB options.

The BRISQUE metric is known to be sensitive to noise and blur by local statistical analysis so that an information loss caused by image processing modules would deteriorate the score. Low scores of our pipeline in Fig. 7 justify that on average our decomposition retains the physical information optimally. Our central sub-aperture images outperform the other two pipelines in 24 out of 36 images of the dataset samples [34]. We achieve a total score of 1567 whereas CLIM-VSENSE yields 1595 and the LFTOOLBOX v0.5 gets 1702 scores. The reason for our strong results relies on our proposed extensions to existing pipelines. This includes the treatment of detected hot-pixels prior to Bayer demosaicing to prevent outliers from propagating to adjacent pixels. We further take advantage of Menon’s method [25] for debayering. In addition, the LFPRESAMPLER contributes to lower scores by conducting micro image alignment in an element-wise manner instead of re-mapping the entire plenoptic image as a whole [37]. Another reason for the improvements is that PLENOPTICAM benefits from insights previously made available by peers such as the de-saturation approach [17]. Apart from that, our automatic histogram alignment based on percentiles of different color spaces tends to be a more generic solution for images of various exposure, which becomes apparent by comparing (h) with (i) in Fig. 8.

For comparisons with the Lytro engine, results were computed with LYTRO DESKTOP v3.4.4 and LYTRO POWER TOOLS v1.0. Thereby, metrics indicate that the latter yields brighter images with larger field of view and allows for numerical parametrization (e.g. λ for focus), making experimental reproduction easier. All Lytro results presented hereafter were

therefore generated using LYTRO POWER TOOLS v1.0.

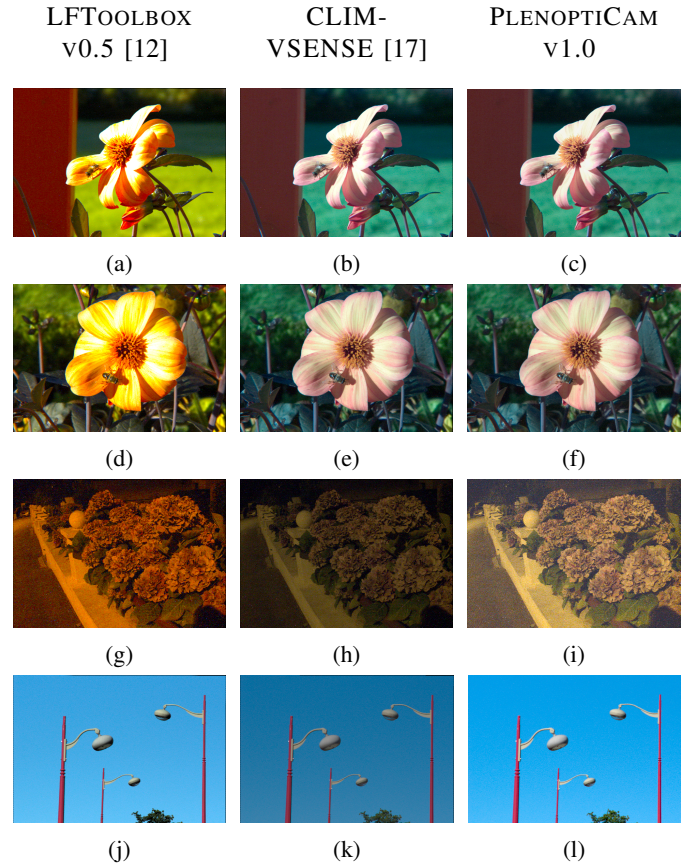


Fig. 8: **Central sub-aperture images** from the IRISA dataset [34] rendered by (left) LFTOOLBOX v0.5 [12], (middle) CLIM-VSENSE [17] and (right) ours for comparison.

LYTRO POWER TOOLS v1.0

PLENOPTICAM v1.0

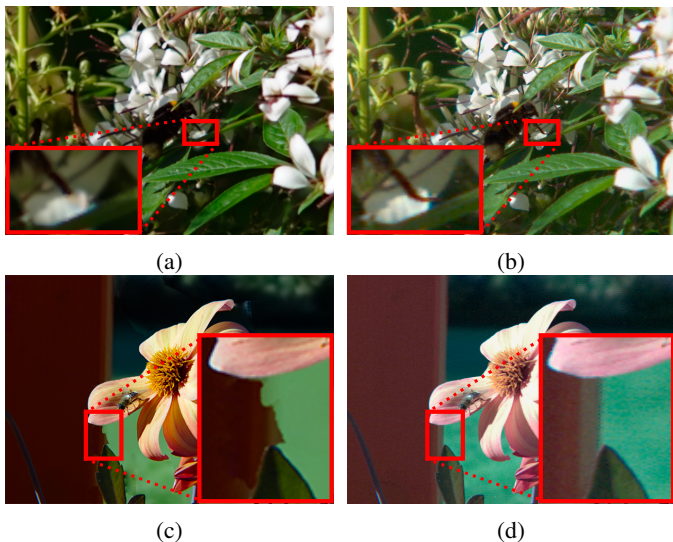


Fig. 9: **View comparison with Lytro engine** revealing differences between classical sub-aperture images (right column) and Lytro’s results (left column), a consequence of all-in-focus rendering from depth-based segmentation [38], [39].

Figure 9 provides a comparison of light-field images rendered by LYTRO POWER TOOLS v1.0 and PLENOPTICAM v1.0, respectively. On closer examination of the Lytro photographs in Figs. 9(a) and 9(c), occasional displacements emerge with image regions being removed or unnaturally shifted from their surroundings. Since Lytro’s code has not been disclosed, the cause for this appearance can only be speculated. A study carried out by scientists formerly affiliated with Lytro suggests that a previously computed depth map is used to fuse a stack of high-resolution refocused frames to an all-in-focus image [38], [39], which in turn may be a starting point for high-resolution angular view synthesis. While this yields higher resolutions, unknown or erroneous disparity is propagated to subsequent stages, i.e. super-resolved views. Image region displacements in Figs. 9(a) and 9(c) thus might be due to false disparities in the depth map. Lytro’s image resolutions are numerically higher than the number of present micro lenses, further supporting the assumption of such pipeline design. These observations bring us to the conclusion that the Lytro engine omits direct access to classical sub-aperture images unlike other available open-source toolchains [12], [17] including ours.

Technically, the user can generate sub-aperture images from Lytro’s aligned ESLF images by completing their processing manually, including pixel rearrangements, adapting angular view positions and accounting for gamma as well as color correction. Given that those ESLF images are at a different processing stage and require additional resources, we compare PLENOPTICAM’s sub-aperture images with the scientific toolbox [12] and its extensions [17]. Nonetheless, we then contrast our refocusing results against those of the Lytro engine in Section III-E.

For further sub-aperture image analysis, we focus on the results of the HEXCORRECTOR where artifacts caused by

hexagonal sampling are subject to removal. Figure 10 shows

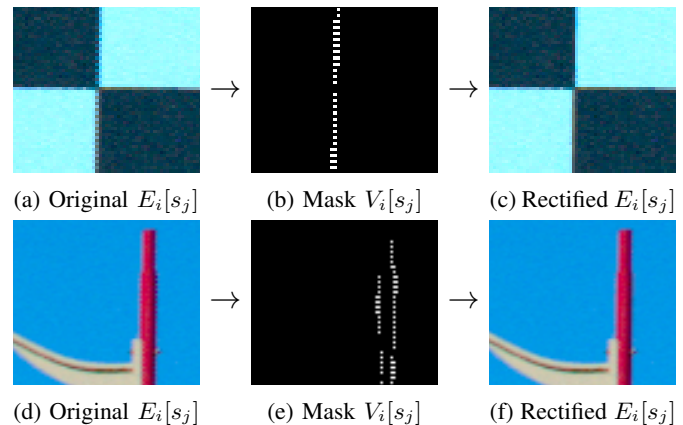


Fig. 10: **Fringe artifact reduction results** showing untreated sub-aperture images in the left column, exhibiting fringes along vertical lines seen upon closer inspection. The binary masks $V_i[s_j]$ indicate detected pixels being sufficiently affected whereas the right column depicts results with smooth edges.

magnified portions of sub-aperture images with apparent fringe artifacts in Figs. 10(a) and 10(d) as well as rectified counterparts exposing smooth edges in Figs. 10(c) and 10(f). Although the efficacy of our treatment is visually notable, this improvement does not present a huge impact on BRISQUE scores. This is likely due to the blind character of the metric and its unawareness of the hexagonal sampling artifact, which can be interpreted as reasonably high spatial frequencies. Another observation made in Fig. 10 is that organic object structures intentionally receive no treatment as they lack straight edges and are thus less affected.

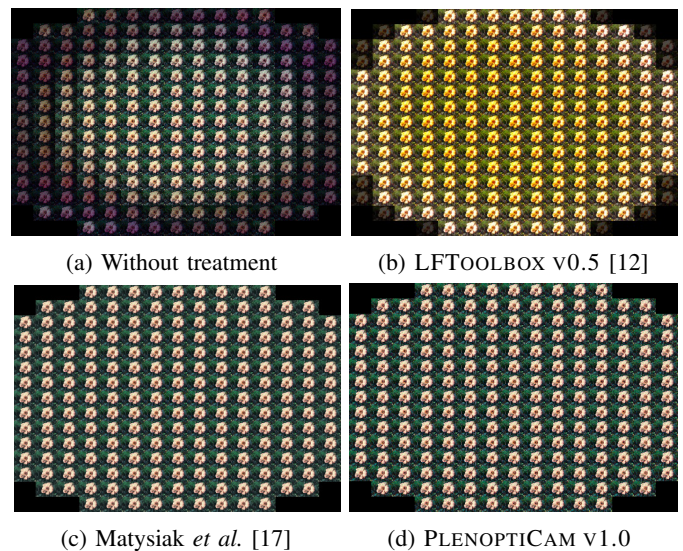


Fig. 11: **Color equalization results** with 15×15 stitched sub-aperture images indicating illumination variances across a decomposed light-field. (a) our result without treatment, (b) Dansereau *et al.* [12], (c) GMM-based method [17] with 240 mins computation time and (d) our HM-MKL compound with 81 secs computation time.

Central sub-aperture images are not the only criterion to describe the quality of a light-field obtained from a plenoptic camera. For instance, rays arriving from non-paraxial angles suffer from natural vignetting causing color inconsistencies within a light-field which we aim to compensate for with the LFP-COLOREQUALIZER module. Figure 11 presents sub-aperture images stitched together for visual inspection of the light-field illumination variances before and after equalization treatment. For better visual analysis, sub-aperture images at a marginal position ($i = 7, g = 2$) are provided in Fig. 12.

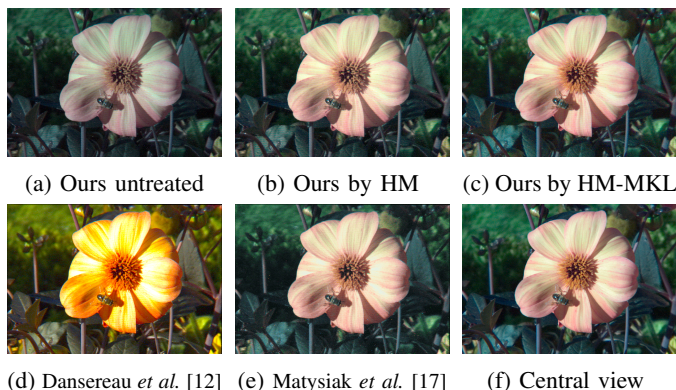


Fig. 12: **Marginal view comparison** of methods combating illumination fall-off at off-axis positions using an exemplary light-field image with $M = 15$. The marginal view location is $i = 7, g = 2$ with (a) the untreated image, (b) after Histogram Matching (HM), (c) from the HM-MKL compound, (d) LFTOOLBOX v0.5 [12], (e) Matysiak *et al.* [17] and (f) the central sub-aperture image ($i = 7, g = 7$) as a reference.

For quantitative assessment of the color transfer we compute the average histogram distance denoted by D using the ℓ^2 norm as given by

$$D = \|f(E_c[s_j]) - f(E_g[s_j])\|_2 \quad (35)$$

where $E_g[s_j]$ represents the marginal and $E_c[s_j]$ the central sub-aperture image serving as the reference while $f(\cdot)$ is the PDF from Eq. (23). Results of our color consistency measurements from Eq. (35) are depicted in Fig. 13.

Computation times of the different sub-aperture decomposition stages are given in Table II. The extensive computational load imposed by Matysiak’s recoloring procedure [17] makes it impractical for us to iterate through an entire dataset.

TABLE II: Computation time comparison where $M = 15$

Process	Dansereau et al.	Matysiak et al.	Ours
De-Multiplexing	70 secs	125 secs	325 secs
Hot Pixel Removal	not supported	100 secs	52 secs
Color Equalization	not supported	234 mins	81 secs
Total	70 secs	237 mins	458 secs

Using the afore-mentioned image metrics, no measurable improvements could be observed from rotating a plenoptic image. Nonetheless, rotation of the 4-D micro image representation proved to be more robust when processing large micro images (e.g. $M = 15$) located at the image border. This is resolved by rotation as it shifts marginal micro images away

from the image border and enables consideration of marginal image pixels.

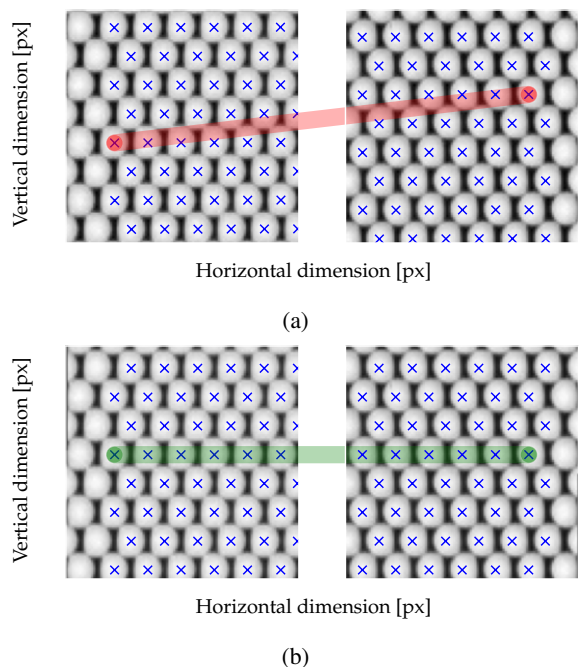
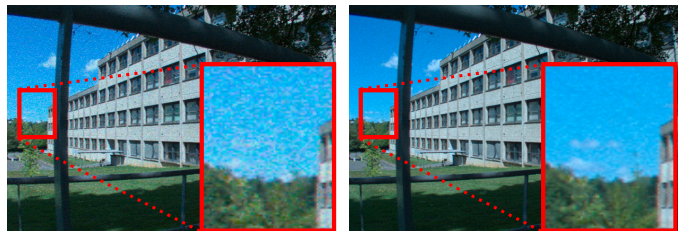


Fig. 14: **Micro image array rotation** with cropped views from a Lytro white image being untreated in (a) and rotated in (b). Transparent lines embrace MICs of the same row near image borders to demonstrate the effectiveness of the LFPROTATOR.

C. De-Vignetting



(a) 74 dB SNR from division (b) 85 dB SNR from LSQ fit

Fig. 15: **De-vignetting** from a white image with Gaussian noise $\sigma = 0.15$. The noise was absent when de-vignetting the ground-truth. Noise propagates to the light-field during division as seen in (a) and significantly suppressed in (b) via patch-wise micro image fitting based on Eqs. (14) to (16). Our approach gains ~ 10 dB of SNR compared to the ordinary division as used by [12], [17].

Experimental validation of our LSQ-based de-vignetting in Eqs. (14) to (16) is assessed using the Signal-to-Noise-Ratio (SNR) given by

$$SNR = 20 \cdot \log_{10} \left(\frac{2^8 - 1}{\sqrt{\frac{1}{J} \sum_{j=1}^J (E_T[s_j] - E_c[s_j])^2}} \right) \quad (36)$$

as a metric to analyse its effectiveness. For the ground-truth data $E_T[s_j]$, we use a photograph divided by a white image

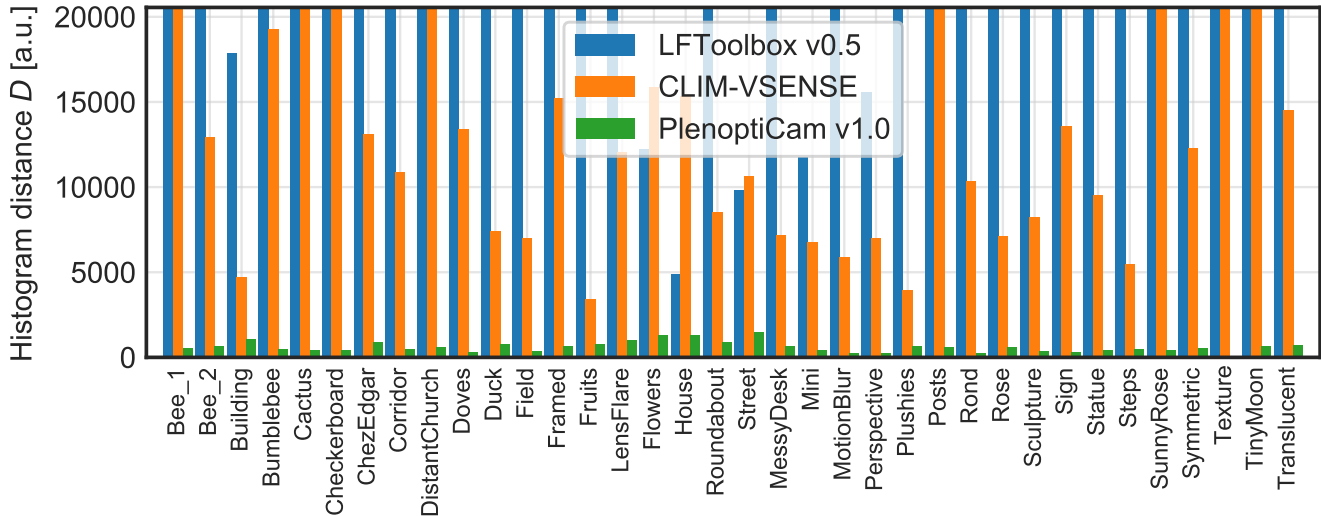


Fig. 13: **Light-field color consistency metric** from histogram distance D with low values indicating higher similarity between marginal views $E_g[s_j]$ at position $i = 7, g = 2$ and corresponding central views $E_c[s_j]$ in light-fields of size $M = 15$.

considered noiseless. This white image is then exposed to additive Gaussian noise with $\sigma = 0.15$ for de-veignetting by either classical division [12], [17] and our proposed fitting scheme. In doing so, we expect the synthetic noise to propagate during de-veignetting, however, with sufficient suppression (i.e. higher SNR) for our LSQ approach. The results in Fig. 15 show that our method retains the image quality by gaining ~ 10 dB of dynamic range with respect to noise. This is a consequence of the least-squares fit treating pixel noise as residuals. Although our evaluation contains highly amplified noise, this method is regarded equally beneficial for low-noise images.

D. Refocusing

For the refocusing assessment, we compare the proposed LFPREFOCUSER module against LYTRO POWER TOOLS v1.0. Refocused images are depicted in Fig. 16. We choose the *Bumblebee.lfp* image from the IRISA dataset [34] as it exhibits organic object structures spread through a wide range of depth.

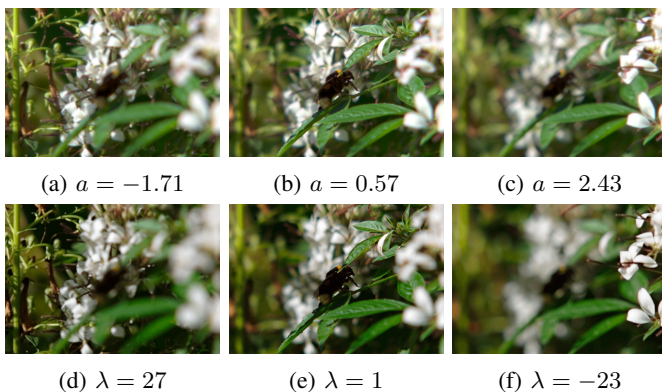


Fig. 16: **Refocused photographs** from PLENOPTICAM v1.0 in the top row with shift and sum parameter a in comparison to results processed by LYTRO POWER TOOLS v1.0 in the bottom row with focus parameter λ .

Quantitative comparison is achieved by analysis of the sharpness and BRISQUE score of local image details. For the sharpness analysis, we follow the Mavridaki and Mezaris [40] approach by transforming cropped versions of a refocused image slice $E_a''[s_j, t_h]$ to the Fourier domain using the Discrete Fourier Transformation (DFT) and extracting the magnitude signal $\mathcal{X}[\sigma_\omega, \rho_\psi]$ by

$$\mathcal{X}[\sigma_\omega, \rho_\psi] = \left| \sum_{j=\xi}^{\Xi} \sum_{h=\varpi}^{\Pi} E_a''[s_j, t_h] \exp(-2\pi\kappa(j\omega/(\Xi - \xi) + h\psi/(\Pi - \varpi))) \right| \quad (37)$$

where $\kappa = \sqrt{-1}$ and $|\cdot|$ yields absolute values. Given the 2-D magnitude signal $\mathcal{X}[\sigma_\omega, \rho_\psi]$, the total energy TE reads

$$TE = \sum_{\omega=1}^{\Omega} \sum_{\psi=1}^{\Psi} \mathcal{X}[\sigma_\omega, \rho_\psi]^2 \quad (38)$$

where $\Omega = \lceil (\Xi - \xi)/2 \rceil$ and $\Psi = \lceil (\Pi - \varpi)/2 \rceil$ are borders cropping the first quarter of the unshifted magnitude signal. To isolate the energy of high frequency elements HE , we compute the power of low frequencies and subtract them from TE which reads

$$HE = TE - \sum_{\omega=1}^{Q_H} \sum_{\psi=1}^{Q_V} \mathcal{X}[\sigma_\omega, \rho_\psi]^2 \quad (39)$$

with Q_H and Q_V as scalar limits in the range of $\{1, 2, \dots, \Omega\}$ and $\{1, 2, \dots, \Psi\}$ separating low from high frequencies. In our experiments we set the limits to a five hundredths of the cropped image resolution. Finally, the sharpness S is a frequency ratio of refocused image portions obtained by

$$S = \frac{HE}{TE} \quad (40)$$

which serves as our blur metric.

From the cropped view of the Lytro image in Fig. 17(l), it is seen that there is no gradual decrease in blur between objects at different depth leading to an unnatural appearance of image blur. Images rendered with LFPREFOCUSER do not expose such sudden change in sharpness. It is only up to speculation on how Lytro’s refocusing algorithm works. The high resolution and occasional blur artifacts around object edges suggest that Lytro employs a super-resolution method at the first stage and then re-blurs spatial areas guided by a previously computed depth map. This may explain blur artifacts at object boundaries, which rely on the quality of a depth map.

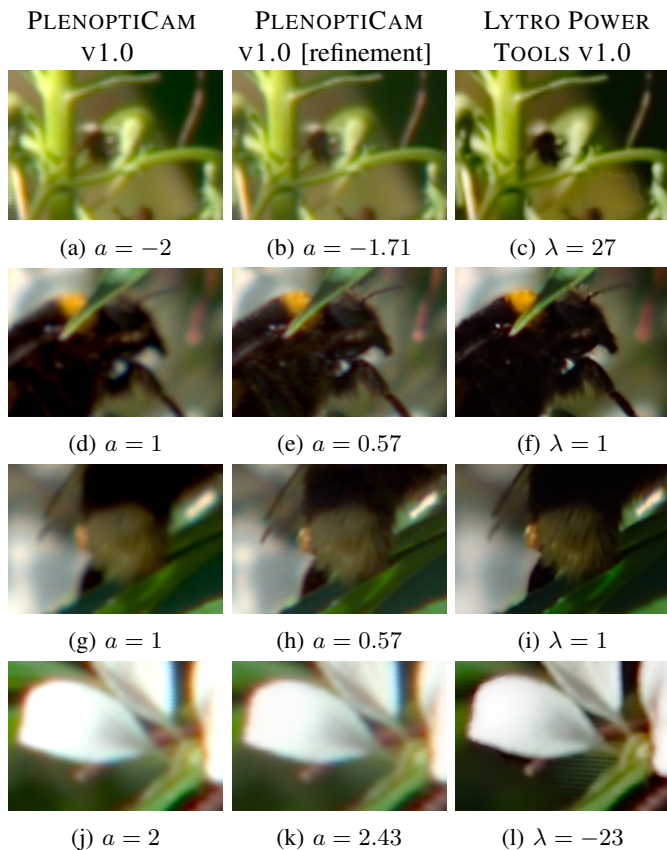


Fig. 17: **Magnified refocused image tiles** showing texture details which are quantified by our blur metric S in Table III. The left and middle column contain results from PLENOPTICAM v1.0 whereas (b), (e), (h), (k) are rendered with sub-pixel precision. The right column is obtained from LYTRO POWER TOOLS v1.0 using focus parameter λ .

It is therefore questionable whether the measured sharpness in Lytro’s refocus algorithm arises from high frequency artifacts. By visual inspection, however, it becomes apparent that the magnified views from Lytro expose more image detail at small λ value. This observation is backed by respective scores from the BRISQUE metric in Table III. On the contrary, occasional artifact patterns as in Fig. 17(l) may still appear unpleasant to the human visual perception.

TABLE III: Metric assessment of refocused images

Fig. 17	(a)	(b)	(c)	(d)	(e)	(f)
Metrics						
Sharpness S	0.034	0.040	0.060	0.107	0.107	0.224
BRISQUE score	84.29	83.51	81.67	92.43	81.29	77.29

Fig. 17	(g)	(h)	(i)	(j)	(k)	(l)
Metrics						
Sharpness S	0.107	0.107	0.125	0.022	0.027	0.054
BRISQUE score	92.43	81.29	81.19	94.30	90.56	80.22

An exemplary result of the LFPSCHEIMPFLUG rendering engine is depicted in Fig. 18. Note how image areas in the upper left background expose sharp details, whereas the focus gradually moves toward the lower right foreground. This is a consequence of the synthetic focus plane being tilted with respect to the image sensor.



Fig. 18: **Scheimpflug rendered photograph** from LFPSCHEIMPFLUG class with $a = \{0, 1\}$ and sub-pixel precision.

V. CONCLUSIONS

Plenoptic image decomposition is a crucial task in light-field rendering for which we propose a pipeline with outstanding image quality. To the best of our knowledge, PLENOPTICAM is the only framework that allows users to automatically calibrate footage from different types of plenoptic cameras regardless of the micro lens specification. We achieve this by employing blob detection, non-maximum suppression and a generic MLA grid geometry recognition. The light-field color equalization stage is taken to a new level by using histogram matching in conjunction with a Monge-Kantorovich solver to yield convincing quantitative results at reasonable computation times, which accelerates a previous method based on Gaussian Mixture Models (GMM) by several orders of magnitude. For plenoptic image alignment, we created an alternative element-wise micro image resampling procedure. Moreover, we are first to address fringe artifacts caused by hexagonal micro lens arrangements, which are successfully reduced by our novel identification scheme. An extensive quantitative assessment of state-of-the-art sub-aperture image decomposition pipelines has been carried out in this paper with the result of outperforming other tool chains in two thirds of the cases, using a wide range of image metrics such as

BRISQUE, average histogram distance via ℓ^2 norm and a blur metric.

These findings and respective implementations are released as an open-source software framework made available as a repository on GitHub [41] to allow others to participate and contribute. The herein presented framework is intended to disburden newcomers and facilitate first steps in the field of plenoptic imaging. Peers are encouraged to report bugs and actively expand this software. PLENOPTICAM may lay the groundwork for future algorithm development and testing of plenoptic data.

Such extensions may include, but are not limited to, an algorithm development for the focused plenoptic camera as initially discovered by Lumsdaine and Georgiev [42]. An implementation of a super-resolution technique may be accomplished on the basis of early pioneering work [43], [38]. It should also be feasible to enhance the image quality by combating optical aberrations as shown in previous studies [44], [45], [46], [39], [47] or by making use of the Bayer demosaicing similar to what Yu and Yu have revealed [48]. Until now, rectification for lens distortions exceeded the scope as this can be accomplished using traditional computer vision libraries. However, correct disparity estimation requires counteracting distortions in sub-aperture images at a preceding stage.

We believe that our work will be a substantial contribution to the field of plenoptic cameras, which is not limited to the image processing community. As Dansereau's LFTOOLBOX has shown, there is a large group of researchers experimenting with plenoptic cameras demonstrating the demand for an easy-to-use software addressing the special requirements for plenoptic imaging. PLENOPTICAM may serve this broad user group including image scientists, programmers in the fields of data science, medical and industrial engineering or photography independent of the user's operating system. In particular, PLENOPTICAM facilitates light-field data preparation for visual machine learning systems such as convolutional neural networks, which currently receive an increasing interest from a variety of scientific and industrial communities. The chosen open source license model enables cost-free usage and code republication with modifications, giving users the opportunity to extend the presented software.

REFERENCES

- [1] R. Ng, M. Levoy, M. Brédif, G. Duval, M. Horowitz, and P. Hanrahan, "Light field photography with a hand-held plenoptic camera," Stanford University, Tech. Rep. CTSR 2005-02, 2005.
- [2] C. Hahne, A. Aggoun, V. Velisavljevic, S. Fiebig, and M. Pesch, "Refocusing distance of a standard plenoptic camera," *Opt. Express*, vol. 24, no. 19, pp. 21 521–21 540, Sep 2016. [Online]. Available: <http://www.opticsexpress.org/abstract.cfm?URI=oe-24-19-21521>
- [3] R. Prevedel, Y.-G. Yoon, M. Hoffmann, N. Pak, G. Wetzstein, S. Kato, T. Schrödel, R. Raskar, M. Zimmer, E. S. Boyden *et al.*, "Simultaneous whole-animal 3d imaging of neuronal activity using light-field microscopy," *Nature methods*, vol. 11, no. 7, p. 727, 2014.
- [4] H. Li, C. Guo, D. Kim-Holzappel, W. Li, Y. Altshuler, B. Schroeder, W. Liu, Y. Meng, J. French, K.-I. Takamaru, M. Frohman, and S. Jia, "Fast, volumetric live-cell imaging using high-resolution light-field microscopy," *bioRxiv*, 2018. [Online]. Available: <https://www.biorxiv.org/content/early/2018/10/10/439315>
- [5] N. Bedard, T. Shope, A. Hoberman, M. Ann Haraman, N. Shaikh, J. Kovačević, N. Balram, and I. Tošić, "Light field otoscope design for 3d in vivo imaging of the middle ear," *Biomedical Optics Express*, vol. 8, p. 260, 01 2017.
- [6] D. W. Palmer, T. Coppin, K. Rana, D. G. Dansereau, M. Suheimat, M. Maynard, D. A. Atchison, J. Roberts, R. Crawford, and A. Jaiprakash, "Glare-free retinal imaging using a portable light field fundus camera," *Biomedical Optics Express*, vol. 9, p. 3178, 07 2018.
- [7] P. P. Srinivasan, T. Wang, A. Sreelal, R. Ramamoorthi, and R. Ng, "Learning to synthesize a 4d rgbd light field from a single image," in *The IEEE International Conference on Computer Vision (ICCV)*, Oct 2017.
- [8] M. Levoy and P. Hanrahan, "Light field rendering," Stanford University, Tech. Rep., 1996.
- [9] E. H. Adelson and J. Y. Wang, "Single lens stereo with a plenoptic camera," *IEEE Transactions on Pattern Analysis and Machine Intelligence*, vol. 14, no. 2, pp. 99–106, February 1992.
- [10] C. Hahne, A. Aggoun, V. Velisavljevic, S. Fiebig, and M. Pesch, "Baseline and triangulation geometry in a standard plenoptic camera," *International Journal of Computer Vision*, vol. 126, no. 1, pp. 21–35, Jan 2018. [Online]. Available: <https://doi.org/10.1007/s11263-017-1036-4>
- [11] D. Cho, M. Lee, S. Kim, and Y.-W. Tai, "Modeling the calibration pipeline of the lytro camera for high quality light-field image reconstruction," in *IEEE International Conference on Computer Vision (ICCV)*, December 2013, pp. 3280–3287.
- [12] D. G. Dansereau, O. Pizarro, and S. B. Williams, "Decoding, calibration and rectification for lenselet-based plenoptic cameras," in *IEEE International Conference on Computer Vision and Pattern Recognition (CVPR)*, June 2013, pp. 1027–1034.
- [13] N. Patel, "lfp-tools," <https://github.com/nrpatel/lfp-tools>, 2011.
- [14] B. Esfahbod, "python-lfp-reader," <https://github.com/behnami/python-lfp-reader>, 2013.
- [15] Y. Bok, H.-G. Jeon, and I. S. Kweon, "Geometric calibration of micro-lens-based light-field cameras using line features," in *Proceedings of European Conference on Computer Vision (ECCV)*, 2014.
- [16] P. David, M. Le Pendu, and C. Guillemot, "White lenslet image guided demosaicing for plenoptic cameras," 10 2017, pp. 1–6.
- [17] P. Matysiak, M. Grogan, M. L. Pendu, M. Alain, and A. Smolic, "A pipeline for lenslet light field quality enhancement," *2018 25th IEEE International Conference on Image Processing (ICIP)*, Oct 2018. [Online]. Available: <http://dx.doi.org/10.1109/ICIP.2018.8451544>
- [18] C. Hahne and A. Aggoun, "Pleptosign: An optical design tool for plenoptic imaging," *SoftwareX*, vol. 10, p. 100259, 2019. [Online]. Available: <http://www.sciencedirect.com/science/article/pii/S2352711019300159>
- [19] Project Jupyter, Matthias Bussonnier, Jessica Forde, Jeremy Freeman, Brian Granger, Tim Head, Chris Holdgraf, Kyle Kelley, Gladys Nalvarez, Andrew Osherooff, M. Pacer, Yuvi Panda, Fernando Perez, Benjamin Ragan Kelley, and Carol Willing, "Binder 2.0 - Reproducible, interactive, sharable environments for science at scale," in *Proceedings of the 17th Python in Science Conference*, Fatih Akici, David Lippa, Dillon Niederhut, and M. Pacer, Eds., 2018, pp. 113 – 120.
- [20] T. Lindeberg, *Scale-Space Theory in Computer Vision*, 01 1994.
- [21] J. L. Crowley, O. Riff, and J. H. Piater, "Fast computation of characteristic scale using a half-octave pyramid," in *In: Scale Space 03: 4th International Conference on Scale-Space theories in Computer Vision, Isle of Skye*, 2002.
- [22] C.-K. Liang and Z. Wang, "Calibration of light-field camera geometry via robust fitting," U.S. Patent 9 420 276 B2, Aug. 2016.
- [23] T. Q. Pham, "Non-maximum suppression using fewer than two comparisons per pixel," in *Advanced Concepts for Intelligent Vision Systems*, J. Blanc-Talon, D. Bone, W. Philips, D. Popescu, and P. Scheunders, Eds. Berlin, Heidelberg: Springer Berlin Heidelberg, 2010, pp. 438–451.
- [24] A. Kordecki, H. Palus, and A. Bal, "Practical vignetting correction method for digital camera with measurement of surface luminance distribution," *Signal, Image and Video Processing*, vol. 10, pp. 1417–1424, 2016.
- [25] D. Menon, S. Andriani, and G. Calvagno, "Demosaicing With Directional Filtering and a posteriori Decision," *IEEE Transactions on Image Processing*, vol. 16, no. 1, pp. 132–141, jan 2007. [Online]. Available: <http://ieeexplore.ieee.org/document/4032820>
- [26] F. Pitié and A. Kokaram, "The linear monge-kantorovitch colour mapping for example-based colour transfer," *IET Conference Proceedings*, pp. 23–23(1), January 2007.
- [27] R. Gonzalez and R. Woods, *Digital Image Processing, Global Editon*. Pearson, 2017.
- [28] F. Pitié, A. Kokaram, and R. Dahyot, ser. Image Processing Series. CRC Press, Sep 2008, ch. Enhancement of Digital Photographs Using Color Transfer Techniques, pp. 295–321, 0. [Online]. Available: <http://dx.doi.org/10.1201/9781420054538.ch11>

- [29] A. Isaksen, “Dynamically reparameterized light fields,” Master’s thesis, Electrical Engineering and Computer Science, Massachusetts Institute of Technology, November 2000.
- [30] C. Hahne, A. Lumsdaine, A. Aggoun, and V. Velisavljevic, “Real-time refocusing using an fpga-based standard plenoptic camera,” *IEEE Transactions on Industrial Electronics*, vol. 65, no. 12, pp. 9757–9766, Dec 2018.
- [31] C. Pitts, T. Knight, C. Liang, and Y. Ng, “Compensating for variation in microlens position during light-field image processing,” August 2013, uS Patent App. 13/774,971. [Online]. Available: <http://www.google.co.uk/patents/US20130222606>
- [32] L. Mignard-Debise and I. Ihrke, “A Vignetting Model for Light Field Cameras with an Application to Light Field Microscopy,” *IEEE Transactions on Computational Imaging*, p. 10, Apr. 2019. [Online]. Available: <https://hal.archives-ouvertes.fr/hal-02263377>
- [33] M. Schambach and F. Puente León, “Microlens array grid estimation, light field decoding, and calibration,” *IEEE transactions on computational imaging*, vol. 6, p. 591–603, 2020.
- [34] R. C. Daudt and C. Guillemot, Lytro illum light field dataset. [Online]. Available: <https://www.irisa.fr/temics/demos/IllumDatasetLF/index.html>
- [35] A. Mittal, A. K. Moorthy, and A. Bovik, “No-reference image quality assessment in the spatial domain,” *IEEE Transactions on Image Processing*, vol. 21, pp. 4695–4708, 2012.
- [36] Bukalapak, “Pybrisque,” <https://github.com/bukalapak/pybrisque>, 2020.
- [37] D. G. Dansereau, O. Pizarro, and S. B. Williams, “Linear volumetric focus for light field cameras,” *ACM Trans. Graph.*, vol. 34, no. 2, pp. 15:1–15:20, Mar. 2015. [Online]. Available: <http://doi.acm.org/10.1145/2665074>
- [38] C.-K. Liang and R. Ramamoorthi, “A light transport framework for lenslet light field cameras,” *ACM Trans. Graph.*, vol. 34, no. 2, Mar. 2015. [Online]. Available: <https://doi.org/10.1145/2665075>
- [39] L.-Y. Wei, C.-K. Liang, G. Myhre, C. Pitts, and K. Akeley, “Improving light field camera sample design with irregularity and aberration,” *ACM Trans. Graph.*, vol. 34, no. 4, Jul. 2015. [Online]. Available: <https://doi.org/10.1145/2766885>
- [40] E. Mavridaki and V. Mezaris, “No-reference blur assessment in natural images using fourier transform and spatial pyramids,” in *2014 IEEE International Conference on Image Processing (ICIP)*, October 2014, pp. 566–570.
- [41] C. Hahne, “Plenopticcam,” <https://github.com/hahne/plenopticcam>, 2020.
- [42] A. Lumsdaine and T. Georgiev, “Full resolution lightfield rendering,” Adobe Systems, Inc., Tech. Rep., January 2008.
- [43] T. E. Bishop, S. Zanetti, and P. Favaro, “Light field superresolution,” in *IEEE International Conference on Computational Photography (ICCP)*, 2009.
- [44] R. Ng, “Digital light field photography,” Ph.D. dissertation, Stanford University, July 2006.
- [45] R. Ng and P. Hanrahan, “Digital correction of lens aberrations in light field photography,” in *International Optical Design Conference*, vol. Proc. SPIE 6342. Stanford University, July 2006. [Online]. Available: <http://dx.doi.org/10.1117/12.692290>
- [46] N. Cohen, S. Yang, A. Andalman, M. Broxton, L. Grosenick, K. Deisseroth, M. Horowitz, and M. Levoy, “Enhancing the performance of the light field microscope using wavefront coding,” *Opt. Express*, vol. 22, no. 20, pp. 24817–24839, Oct 2014. [Online]. Available: <http://www.opticsexpress.org/abstract.cfm?URI=oe-22-20-24817>
- [47] C.-K. Liang, C. Pitts, C. Craddock, and G. Myhre, “Light-field aberration correction,” U.S. Patent 9 628 684 B2, Apr. 2017.
- [48] Z. Yu, J. Yu, A. Lumsdaine, and T. Georgiev, “An analysis of color demosaicing in plenoptic cameras,” in *IEEE International Conference on Computer Vision and Pattern Recognition (CVPR)*, 2012, pp. 901–908.

APPENDIX A SCALE SPACE THEOREM

Proof. Let $G(\sigma, \mathbf{x})$ be a Gaussian function of $\mathbf{x} = \{x, y\} \in \mathbb{R}^2$ and σ the scale of interest in a Laplacian pyramid, so that

$$G(\sigma, x, y) = e^{-\frac{x^2+y^2}{2\sigma^2}}$$

$$\partial_x G(\sigma, x, y) = -\frac{x}{\sigma^2} e^{-\frac{x^2+y^2}{2\sigma^2}}$$

$$\partial_{xx} G(\sigma, x, y) = -\frac{x}{\sigma^2} e^{-\frac{x^2+y^2}{2\sigma^2}} + \frac{x}{\sigma^4} e^{-\frac{x^2+y^2}{2\sigma^2}}$$

$$\begin{aligned} \nabla^2 G(\sigma, x, y) &= \partial_{xx} G(\sigma, x, y) + \partial_{yy} G(\sigma, x, y) \\ &= \left(\frac{x^2+y^2}{\sigma^4} - \frac{2}{\sigma^2} \right) e^{-\frac{x^2+y^2}{2\sigma^2}} \end{aligned}$$

$$r^2 = x^2 + y^2$$

$$0 = \frac{r^2}{\sigma^4} - \frac{2}{\sigma^2}$$

$$r^2 = 2\sigma^2$$

$$r = \sqrt{2}\sigma$$

$$M \approx 2r = 2\sqrt{2}\sigma \quad \square$$



Christopher Hahne is a visiting scholar affiliated with the School of Mathematics and Computer Science at the University of Wolverhampton. He received the BSc degree in 2012 from the University of Applied Sciences Hamburg while working at R&D departments of Rohde & Schwarz GmbH & Co. KG as well as ARRI Cinetechnik GmbH & Co. KG. After becoming a visiting student at Brunel University in 2012, he transferred to a bursary-funded PhD programme and was awarded the doctoral degree in Computer Science from the University of Bedfordshire in 2016. His research interests include algorithm development for audio-visual content.



Amar Aggoun is currently the Head of School of Mathematics and Computer Science and Professor of Visual Computing at the University of Wolverhampton. He received the “Ingenieur d’état” degree in Electronics Engineering in 1986 from Ecole Nationale Polytechnique d’Alger (Algiers, Algeria) and a PhD degree in Electronic Engineering from the University of Nottingham. His academic career started at the University of Nottingham where he held the positions of research fellow in low power DSP architectures and visiting lecturer in Electronic Engineering and Mathematics. In 1993 he joined De Montfort University as a lecturer and progressed to the position of Principal Lecturer in 2000. In 2005 he joined Brunel University as Reader in Information and Communication Technologies. From 2013 to 2016, he was at the University of Bedfordshire as Head of School of Computer Science and Technology. He was also the director of the Institute for Research in Applicable Computing which oversees all the research within the School. His research is mainly focused on 3D Imaging and Immersive Technologies and he successfully secured and delivered research contracts worth in excess of £6.9M, funded by the research councils UK, Innovate UK, the European commission and industry. Amongst the successful project, he was the initiator and the principal coordinator and manager of a project sponsored by the EU-FP7 ICT-4.1.5-Networked Media and 3D Internet, namely Live Immerse Video-Audio Interactive Multimedia (3D VIVANT). He holds three filed patents, published more than 200 peer-reviewed journals and conference publications and contributed to two white papers for the European Commission on the Future Internet. He also served as Associate Editor for the IEEE/OSA Journal of Display Technologies.